

# AURASeg: Attention-guided Upsampling with Residual-Assistive Boundary Refinement for Onboard Robot Drivable-Area Segmentation

Narendhiran Vijayakumar  
NIT Tiruchirappalli  
narendhiranv.nitt@gmail.com

Sridevi M  
NIT Tiruchirappalli  
msridevi@nitt.edu

## Abstract

Free space ground segmentation is essential to navigate autonomous robots, recognize drivable zones, and traverse efficiently. Fine-grained features remain challenging for existing segmentation models, particularly for robots in indoor, outdoor and road-scene environments. These difficulties arise from ineffective multi-scale processing, sub-optimal boundary refinement, and limited feature representation. To address this, we propose Attention-guided Upsampling with Residual-Assistive Boundary Refinement (AURASeg), a ground-plane drivable area segmentation framework designed to improve boundary precision while preserving strong region accuracy under edge-deployment constraints. Built on ResNet backbone, we propose (i) a Residual Boundary Refinement Module (RBRM) that enhances edge delineation through boundary-assistive feature refinement, and (ii) Attention Progressive Upsampling Decoder (APUD) blocks that fuse multi-level features using residual fusion of attention modules; additionally, we integrate (iii) a lightweight ASPPLite module to capture multi-scale context with minimal overhead. Extensive experiments on CARL-D, the Ground Mobile Robot Perception (GMRPD) dataset, and a custom Gazebo indoor dataset show that AURASeg consistently outperforms strong baselines, with notable gains in boundary metrics. Finally, we demonstrate on-device deployment on a Jetson Nano powered Kobuki TurtleBot, validating practical edge-inference feasibility. Code will be made publicly available.

## 1. Introduction

Autonomous robotic navigation relies on semantic segmentation to understand surrounding scenes with high precision, enabling safe and efficient motion planning. Despite substantial progress in deep learning-based segmentation architectures, key challenges remain in feature representation, multi-scale learning, and boundary precision, limiting deployment reliability in real-time robotic systems. In practi-

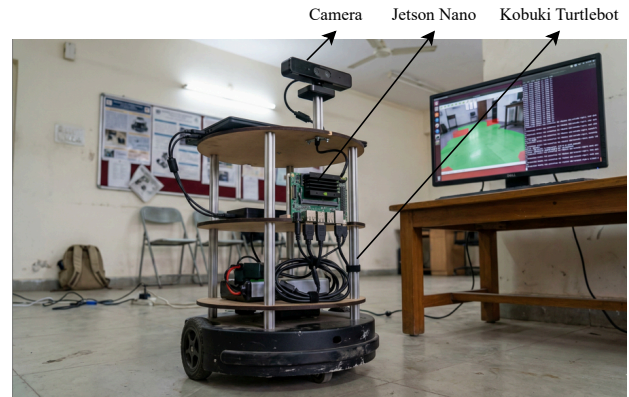


Figure 1. Onboard inference of drivable-area segmentation on a Kobuki TurtleBot2 using NVIDIA Jetson Nano.

cal robotic settings, segmentation models must also operate under tight resource and latency constraints to support onboard edge deployment. Feature extraction and fusion are especially critical because they directly influence segmentation robustness under viewpoint changes, clutter, and illumination variation.

Traditional segmentation methods such as DeepLab [1] and DeepLabv3+ [2] introduced Atrous Spatial Pyramid Pooling (ASPP), which captures multi-scale contextual information through dilated convolutions with different receptive fields. Subsequent works such as FBRNet [3] improved pyramid-based aggregation by incorporating reinforced spatial pooling to reduce computational overhead while improving segmentation quality. In parallel, efficient feature fusion and boundary refinement strategies have been explored in architectures such as BiSeNet [4] and FPANet [5], which leverage residual connections and multi-branch designs to improve edge precision. More broadly, recent segmentation research has emphasized lightweight and efficient designs for robotics applications, highlighting the importance of balancing accuracy, boundary quality, and computational cost.

However, boundary refinement still remains a recurring issue in segmentation: poor boundary delineation often causes misclassified pixels near object edges, reducing the reliability of segmentation-based navigation. For mobile robot perception, such boundary artifacts can propagate into planning as false obstacles or missing free space, producing overly conservative or unsafe trajectories. This problem is especially evident in drivable-area perception across robotic and road-scene settings, where free-space boundaries can become ambiguous under different environment conditions.

Multi-task learning has also contributed to stronger feature representation; for instance, YOLOP [6], designed for panoptic prediction, demonstrates how shared representations across tasks can improve segmentation performance. Nevertheless, because such models are primarily optimized for panoptic outputs, they are not always ideal for pure semantic segmentation where boundary fidelity is critical for accurate robotic navigation on edge devices. To address these challenges, we propose AURASeg (*Attention-guided Upsampling with Residual-Assistive Boundary Refinement*) and validate through on-device deployment on a Kobuki TurtleBot2 powered by an NVIDIA Jetson Nano, reporting resource-constraint metrics alongside segmentation performance.

Our contributions include:

1. *Residual Boundary Refinement Module (RBRM)*, a refinement head that leverages a Sobel edge prior and gated residual fusion to sharpen contours and improve boundary-centric metrics.
2. *Attention Progressive Upsampling Decoder (APUD)*, an attention-guided decoder that progressively upsamples and fuses multi-scale features to recover fine-grained spatial structure.
3. *ASPPLite*, a lightweight multi-scale context module that enriches bottleneck features with minimal computational overhead.

## 2. Related Work

Semantic segmentation is a critical component of autonomous navigation, allowing robots to detect and separate drivable areas from obstructions. A backbone’s ability to retain spatial structure while extracting high-level context strongly influences segmentation quality. Recent designs have explored improved encoder-decoder alignment and feature selection. Ghost-UNet [7] adopts an asymmetrical encoder–decoder structure to enhance feature alignment, a dual-stream encoder structure is explored in [8], and LCDNet [9] uses gating mechanisms to dynamically select informative features. Across many segmentation families, residual connections [10] remain a common choice to preserve low-level spatial cues and stabilize optimization in deeper networks. Meanwhile, recent segmentation research increasingly emphasizes lightweight and resource-efficient

designs for practical deployment on edge robotic platforms.

Multi-scale context aggregation is equally important, as it enables a model to combine broad receptive fields with fine-grained spatial detail. ASPP captures multi-scale context via parallel dilated convolutions, improving segmentation performance in challenging scenes. Building on this idea, FBRNet [3] enhances multi-scale extraction using reinforced spatial pooling without incurring excessive computational cost. Beyond purely RGB cues, Depth-Guided DPT [11] incorporates depth-aware segmentation and improves feature extraction in robotic perception scenarios where depth information is informative. Another approach is S2-FPN [12], which introduces scale-aware strip-attention connections to refine multi-scale feature selection and strengthen cross-scale fusion.

Attention mechanisms further complement multi-scale aggregation by selectively emphasizing task-relevant features. Self-attention has been shown to improve representation learning in transformer-based and multimodal fusion segmentation models, especially in complex scenes where long-range dependencies matter. TwinLiteNet [13] introduces dual-attention designs with a focus on lane recognition and outdoor drivable-area segmentation, while attention-based refinement blocks [14] improve feature retention during upsampling and reduce spatial artifacts during resolution recovery.

Finally, boundary precision remains a key determinant of navigation reliability, since misclassified pixels along edges can induce planning errors. BASNet [15] proposes an encoder–decoder residual-learning formulation that reinforces edge clarity, and Street Floor Segmentation [16] explores adaptive filtering for refining segmentation masks. Temporal consistency and uncertainty handling have also been studied for mobile robotics. D-Flow [17] introduces Memory-Gated Units (MGUs) to maintain segmentation consistency over sequential frames, and AGSL-Free Driving Region Detection [18] employs uncertainty-aware depth learning to better adapt to low-confidence regions. In contrast to addressing these aspects in isolation, our method consolidates these design choices into a unified framework tailored for boundary-sensitive and resource-constrained free-space segmentation, deployed on a Kobuki TurtleBot2, as shown in Fig. 1.

## 3. Proposed Method

### 3.1. Architecture Overview

As depicted in Fig. 2, AURASeg follows an encoder–decoder architecture tailored for free-space (drivable-area) segmentation in robotic navigation. The input image is first encoded by a ResNet-18 backbone to produce hierarchical feature maps at multiple resolutions. At the bottleneck, ASPPLite aggregates lightweight multi-scale con-

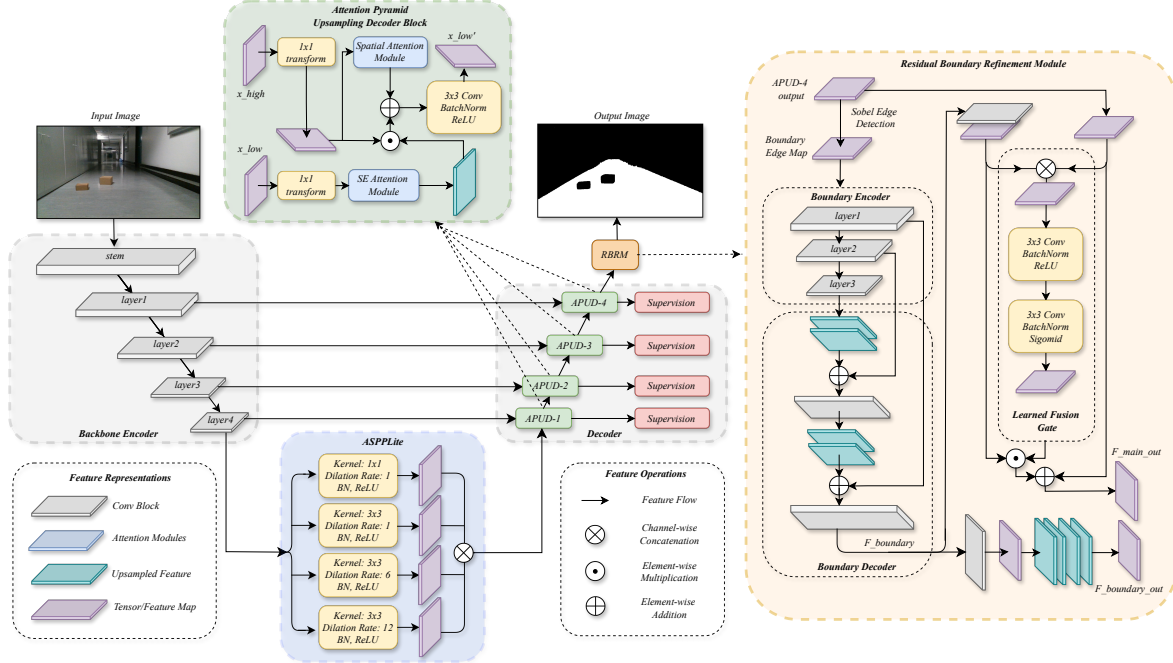


Figure 2. Overview of the proposed free-space drivable area segmentation encoder-decoder network architecture.

text to improve global scene understanding without incurring heavy computation. The decoder then employs APUD blocks to progressively upsample and fuse encoder features, recovering spatial detail and producing a coarse free-space prediction. Finally, RBRM refines this prediction by injecting boundary-sensitive corrections through gated residual fusion, improving contour alignment while preserving interior-region stability.

### 3.2. Encoder Backbone

We use an ImageNet-pretrained ResNet-18 encoder to extract hierarchical features for drivable-area segmentation. Early stages capture low-level cues (e.g., edges and textures), while deeper stages encode high-level semantics. Multi-scale features are forwarded to the decoder through skip connections to recover spatial details during progressive upsampling.

### 3.3. ASPPLite Module

ASPPLite provides multi-scale contextual cues at the bottleneck while keeping computation low for onboard robotic segmentation. It comprises four parallel branches: one  $1 \times 1$  projection branch and three  $3 \times 3$  atrous-convolution branches with dilation rates 1, 6, and 12, each followed by Batch Normalization and ReLU. The  $d=1$  branch preserves local structure, whereas  $d=6$  and  $d=12$  expand the receptive field to capture mid- and long-range context, improving robustness to texture changes, illumination variation, and scene clutter.

Unlike standard ASPP variants that include additional dilation branches and a global average pooling path, ASPPLite omits global pooling to avoid spatial collapse and retain boundary-sensitive information, which is important for ground-plane edges and thin obstacle contours. The branch outputs are concatenated to form a richer multi-scale feature tensor that is forwarded to the decoder.

### 3.4. Attention Progressive Upsampling Decoder (APUD)

Each APUD block fuses a deep, low-resolution semantic feature map  $x_{\text{low}} \in \mathbb{R}^{B \times C_{\ell} \times H_{\ell} \times W_{\ell}}$  with a shallow, high-resolution detail feature map  $x_{\text{high}} \in \mathbb{R}^{B \times C_h \times H_h \times W_h}$  to progressively reconstruct segmentation details. Both inputs are first aligned to a shared embedding dimension  $C$  using lightweight  $1 \times 1$  projections. The semantic branch is then enhanced via Squeeze-and-Excitation (SE) channel attention [19] and bilinearly upsampled to the skip-feature resolution.

To perform selective fusion, APUD applies element-wise multiplication between the upsampled semantic signal and the high-resolution skip feature, acting as a content-dependent gate that suppresses irrelevant textures while retaining boundary-relevant responses. In parallel, the skip branch is refined by a spatial-attention mask [20]. The gated feature and spatially attended skip feature are combined by addition and refined with a  $3 \times 3$  Conv-BN-Act block, producing  $y \in \mathbb{R}^{B \times C \times H_h \times W_h}$ .

$$L = T_\ell(x_{\text{low}}), \quad H = T_h(x_{\text{high}}), \quad (1)$$

$$L' = \mathcal{U}(\text{SE}(L)), \quad F = L' \odot H, \quad S = \text{SA}(H), \quad (2)$$

$$y = R(F + S), \quad (3)$$

where  $T_\ell(\cdot)$  and  $T_h(\cdot)$  are  $1 \times 1$  Conv-BN-Act projections,  $\mathcal{U}(\cdot)$  denotes bilinear upsampling to  $(H_h, W_h)$ ,  $\text{SE}(\cdot)$  is channel attention,  $\text{SA}(\cdot)$  is spatial attention,  $\odot$  denotes element-wise multiplication, and  $R(\cdot)$  is a  $3 \times 3$  Conv-BN-Act refinement.

### 3.5. Residual Boundary Refinement Module (RBRM)

RBRM is placed after the final APUD stage to improve boundary precision in the predicted free-space mask. Although APUD progressively reconstructs features, boundary errors can still occur due to upsampling and ambiguity near thin structures or strong texture transitions (e.g., floor-wall boundaries and obstacle contours). RBRM introduces an explicit boundary-focused branch and merges its cues back into the main decoder stream through gated residual fusion.

Let the APUD output be  $\mathbf{F} \in \mathbb{R}^{C \times H \times W}$  (with  $C=256$  at  $H/4$  resolution in our setting). RBRM first extracts edge-aware features with a lightweight boundary head. The main feature map is projected ( $256 \rightarrow 64$ ), passed through fixed Sobel filters per channel to obtain horizontal and vertical responses, and then fused by a small learnable convolution to form an edge-sensitive tensor  $\mathbf{E} \in \mathbb{R}^{64 \times H \times W}$ .

These features are processed by a compact encoder-decoder pathway. The boundary encoder applies strided convolutions to obtain multi-level boundary representations  $(\mathbf{s}_1, \mathbf{s}_2, \mathbf{s}_3)$ , and the decoder reconstructs them with bilinear upsampling. At each stage, upsampled decoder features are concatenated with corresponding encoder features and refined by convolution blocks, yielding boundary features  $\mathbf{B} \in \mathbb{R}^{64 \times H \times W}$ . The boundary feature map is projected to match the main-stream dimensionality,  $\mathbf{P} = \phi(\mathbf{B}) \in \mathbb{R}^{C \times H \times W}$ , and fused through a learned gate:

$$\mathbf{G} = \sigma(\text{Conv}_{1 \times 1}([\mathbf{F}, \mathbf{P}]]), \quad \mathbf{F}_{\text{ref}} = \mathbf{F} + \mathbf{G} \odot \mathbf{P}, \quad (4)$$

where  $[\cdot, \cdot]$  denotes channel concatenation,  $\sigma(\cdot)$  is the sigmoid function, and  $\odot$  is element-wise multiplication. This gating injects boundary cues only where needed while preserving stable interior regions. In addition to refined features  $\mathbf{F}_{\text{ref}}$  for the final segmentation head, RBRM also outputs an auxiliary boundary map via a  $1 \times 1$  prediction layer on  $\mathbf{B}$  to encourage boundary-aware learning.

### 3.6. Multi-Loss Supervision and Training

As summarized in Tab. 1, we train AURASeg at an input resolution of  $384 \times 640$  using an ImageNet-pretrained

Table 1. Training configuration for AURASeg.

Hyperparameter	Value
<i>Optimization &amp; schedule</i>	
Input resolution	$384 \times 640$
Encoder backbone	ResNet-18
Optimizer	AdamW ( $\beta_1=0.9, \beta_2=0.999$ )
Weight decay	0.01
Learning rate (enc/dec)	$1 \times 10^{-4} / 1 \times 10^{-3}$
Scheduler	Cosine annealing
Epochs	50 (early stop patience: 10)
Batch size	8
Mixed precision	FP16 (AMP)
<i>Loss functions</i>	
Main loss (region)	$0.5 \mathcal{L}_{\text{Focal}} + 0.5 \mathcal{L}_{\text{Dice}}$
Boundary loss	$0.2 \mathcal{L}_{\text{BCE}}$
Auxiliary loss	$0.1 (\mathcal{L}_{\text{Focal}} + \mathcal{L}_{\text{Dice}}) \times 4$
<i>Augmentation</i>	
Horizontal flip	0.5 -
Geometric (shift/scale/rotate)	0.5 shift=0.1, scale=0.1, rot= $\pm 15^\circ$
Brightness + contrast	0.3 $\Delta b = \pm 0.2, \Delta c = \pm 0.2$
Gaussian noise	0.2 var_limit=(10, 50)
Normalize	1.0 ImageNet mean/std

ResNet-18 encoder. We optimize the network with AdamW and differential learning rates:  $1 \times 10^{-4}$  for the encoder and  $1 \times 10^{-3}$  for decoder-side modules (ASPPLite, APUD, RBRM, and segmentation head). A cosine-annealing schedule is applied for up to 50 epochs with early stopping (patience = 10) based on validation performance. Training uses batch size 8 and mixed precision (FP16/AMP) on a single NVIDIA GeForce RTX 5060 GPU. All baseline models are trained under the same input resolution, augmentation pipeline, optimizer family, batch size, and evaluation protocol for fair comparison.

AURASeg is trained with three complementary supervision signals: (i) region loss on the main prediction, (ii) deep supervision on intermediate APUD outputs, and (iii) boundary-specific loss for the RBRM output. Let  $Y$  denote the ground-truth mask and  $\hat{Y}$  the main logits (resized to ground-truth resolution before loss computation). Let  $\hat{Y}^{(k)}$  denote the  $k$ -th auxiliary logits from APUD for  $k \in \{1, \dots, 4\}$ , also resized to ground-truth resolution. The total objective is

$$\mathcal{L} = \mathcal{L}_{\text{main}} + \lambda_{\text{bnd}} \mathcal{L}_{\text{BCE}} + \sum_{k=1}^4 \lambda_{\text{aux}} \mathcal{L}_{\text{aux}}^{(k)}, \quad (5)$$

where  $\lambda_{\text{bnd}} = 0.2$  and  $\lambda_{\text{aux}} = 0.1$  (Tab. 1).

**Main region loss.** We combine Focal loss and Dice loss to balance class-imbalance robustness and overlap-driven optimization:

$$\mathcal{L}_{\text{main}} = 0.5 \mathcal{L}_{\text{Focal}}(\hat{Y}, Y) + 0.5 \mathcal{L}_{\text{Dice}}(\hat{Y}, Y). \quad (6)$$

Table 2. Overview of datasets used for drivable-area segmentation.

Dataset	Environment	Train	Val	Test	Total
Gazebo (ours)	Indoor lab corridors (simulation)	2483	294	420	3197
GMRPD [21]	Outdoor sidewalks, plazas, squares	616	74	110	800
CARL-D [22]	On-road driver-view scenes for autonomous driving	9000	2400	2300	14700

Table 3. Ablation study with ResNet-18 backbone

Variant	ASPPLite	APUD	BRRM	Params (M)	Acc.	B. Acc.
V1: Base (ResNet-18)				14.61	0.9928	0.7804
V2: V1 + ASPPLite	✓			17.98	0.9928	0.7931
V3: V2 + APUD	✓	✓		18.21	0.9943	0.8224
V4: V3 + RBRM (proposed)	✓	✓	✓	<b>23.30</b>	<b>0.9946</b>	<b>0.8504</b>

**Auxiliary deep supervision.** Each intermediate APUD output is supervised with the same region criterion:

$$\mathcal{L}_{\text{aux}}^{(k)} = \mathcal{L}_{\text{Focal}}(\hat{Y}^{(k)}, Y) + \mathcal{L}_{\text{Dice}}(\hat{Y}^{(k)}, Y). \quad (7)$$

**Boundary loss for RBRM.** RBRM predicts a boundary-logit map  $\hat{B}$  (upsampled to ground-truth resolution). The target  $B$  is derived from  $Y$  via a thin edge band (*e.g.*, morphological gradient). Let  $p_i = \sigma(\hat{B}_i)$ . The boundary loss is

$$\mathcal{L}_{\text{BCE}} = -\frac{1}{N} \sum_{i=1}^N \left( B_i \log p_i + (1 - B_i) \log(1 - p_i) \right), \quad (8)$$

where  $N$  is the number of pixels. This objective promotes both region consistency and sharp boundary alignment for drivable-area segmentation in robotic scenes.

## 4. Results

### 4.1. Datasets

As summarized in Tab. 2, we use three datasets to evaluate drivable-area segmentation across heterogeneous environments: (i) a synthetic indoor Gazebo dataset collected for robot navigation, (ii) GMRPD [21], which represents real outdoor traversal scenes for ground robots (*e.g.*, sidewalks and plazas), and (iii) CARL-D [22], which represents road-scene segmentation in autonomous driving.

The Gazebo and GMRPD datasets are jointly treated as the **MIX** split to evaluate free-space segmentation under mixed simulated and real robotic conditions. In contrast, CARL-D is used as a separate benchmark to assess cross-domain generalization to road-scene drivable-area segmentation. Together, these datasets cover indoor, outdoor, and road-scene settings, enabling broad evaluation of boundary-sensitive free-space perception.

### 4.2. Performance Analysis

#### 4.2.1. Ablation Study

Tab. 3 presents a step-wise ablation of the proposed model. Accuracy (Acc.) denotes pixel-wise classification accuracy, and Boundary Accuracy (B. Acc.) denotes Boundary F1 computed on boundary pixels extracted via morphological dilation–erosion operations.

Adding ASPPLite (V2) modestly increases parameters while improving boundary accuracy (0.7804  $\rightarrow$  0.7931), indicating stronger multi-scale context aggregation without degrading region-level accuracy. Introducing APUD (V3) yields the largest boundary gain (0.7931  $\rightarrow$  0.8224) and also improves overall accuracy (0.9928  $\rightarrow$  0.9943), highlighting the benefit of attention-guided skip fusion during reconstruction. Finally, incorporating boundary refinement (V4, proposed) further improves boundary accuracy to 0.8504 with moderate additional computation, confirming that explicit boundary-focused refinement complements ASPPLite and APUD.

To visualize these improvements, Fig. 3 shows a qualitative comparisons across ablation stages. ASPPLite improves global free-space consistency through richer bottleneck context, APUD contributes the strongest recovery of fine spatial details, and RBRM sharpens thin contours and difficult transitions. These qualitative trends are consistent with the quantitative gains.

#### 4.2.2. Metric Evaluation

Tab. 4 summarizes benchmark performance on the MIX (Gazebo+GMRPD) validation set and CARL-D test set. Performance is reported at batch size 1 and input resolution  $384 \times 640$ . All metrics were obtained in 10W MAXN mode using JetPack 4.6.1 (CUDA 10.2, cuDNN 8.2), batch size 1, FP32 PyTorch 1.10 inference, averaged over 500 forward passes after 50 warm-up iterations.

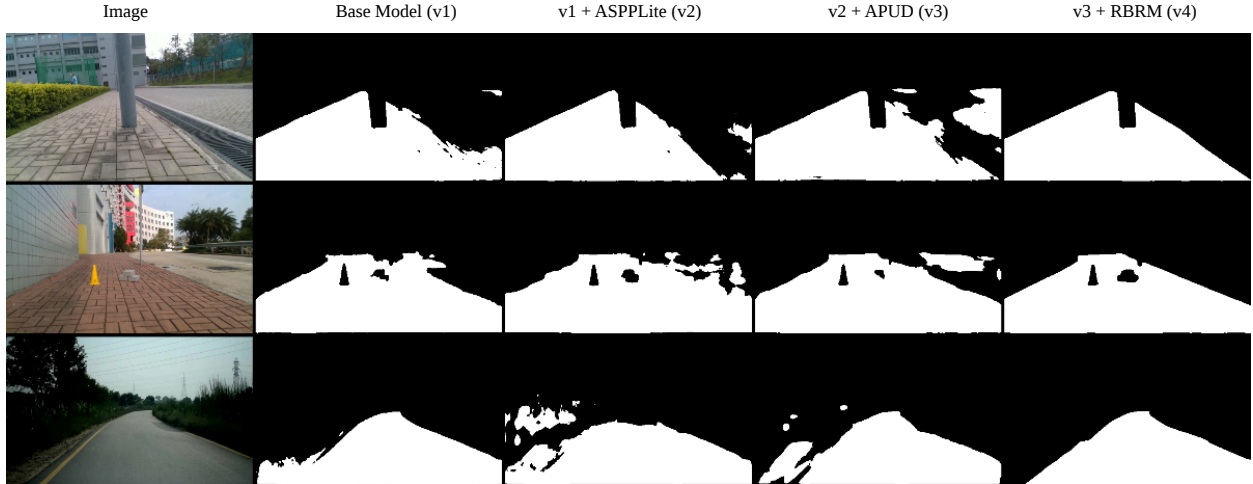


Figure 3. Qualitative comparison across ablation stages (V1–V4)

Table 4. Unified evaluation of proposed AURASeg model on MIX (Gazebo+GMRPD) and CARL-D test set.

Model	MIX (Gazebo+GMRPD)						CARL-D					
	IoU	F1	BIoU	BF1	Prec.	Rec.	IoU	F1	BIoU	BF1	Prec.	Rec.
FCN	0.9857	0.9928	0.6502	0.7789	0.9919	0.9936	0.7735	0.8723	0.0298	0.0448	0.8457	0.9006
PSPNet	0.9870	0.9935	0.7639	0.8589	0.9941	0.9929	0.7835	0.8786	0.0422	0.0624	0.8594	0.8987
DeepLabV3+	0.9875	0.9937	0.7799	0.8700	0.9938	0.9936	0.8012	0.8896	0.0416	0.0597	0.8481	0.9354
UPerNet	0.9879	0.9939	0.7863	0.8738	0.9948	0.9931	0.7965	0.8868	0.0240	0.0371	0.8333	<b>0.9475</b>
SegFormer	0.9885	0.9942	0.7763	0.8683	0.9958	0.9927	0.7675	0.8685	0.0184	0.0316	<b>0.8613</b>	0.8758
Mask2Former	0.9881	0.9940	0.7740	0.8661	0.9955	0.9925	0.7721	0.8714	0.0183	0.0298	0.8284	0.9190
PIDNet	0.9835	0.9917	0.6334	0.7656	0.9912	0.9922	0.7979	0.8876	0.0408	0.0616	0.8580	0.9192
<b>AURASeg (Ours)</b>	<b>0.9897</b>	<b>0.9948</b>	<b>0.8124</b>	<b>0.8905</b>	<b>0.9959</b>	<b>0.9937</b>	<b>0.8041</b>	<b>0.8914</b>	<b>0.0484</b>	<b>0.0683</b>	0.8534	0.9330

Note: Best results per metric within each dataset are highlighted in bold. Boundary metrics are computed using boundary dilation = 2. Boundary metrics on CARL-D are not directly comparable to MIX due to polygon annotation granularity (see Sec. 4.2.2).

Table 5. On-device deployment comparison on NVIDIA Jetson Nano 4GB.

Model	Params (M)	GFLOPs	Peak Memory (MB)	Latency (ms)	FPS
FCN	35.31	139.25	265.5	843.2	1.19
DeepLabV3+	26.68	34.60	230.9	248.7	4.02
UPerNet-R50	37.28	71.93	478.2	523.4	1.91
SegFormer-B2	24.72	19.86	285.4	418.6	2.39
PIDNet-S	36.94	32.35	192.3	210.3	4.76
<b>AURASeg</b>	23.3	134.68	415.7	782.5	1.28

In addition to segmentation metrics, Tab. 5 reports deployment-oriented measures including GFLOPs, parameter count, peak memory, and inference latency on the NVIDIA Jetson Nano 4GB constrained to 472 GFLOPs (FP16) throughput and 25.6 GB/s memory bandwidth. Notably, despite AURASeg having higher computational cost (134.68 GFLOPs), it outperforms FCN (139.25 GFLOPs)

in both latency and accuracy. SegFormer-B2, while having the lowest theoretical GFLOPs (19.86), exhibits disproportionately high latency on the Nano due to the poor hardware utilization of its multi-head layers on the Maxwell GPU architecture, which lacks dedicated tensor cores and is constrained by limited memory bandwidth. PIDNet-S achieves the highest throughput due to its purely convo-

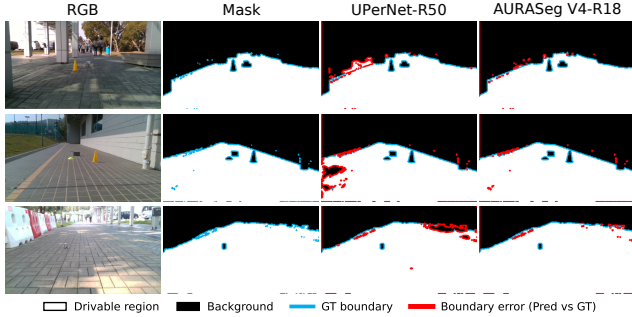


Figure 4. Qualitative comparison with boundary-error overlays (red) and ground truth boundary (blue) for UPerNet and AURASeg models

lutional, three-branch design optimized for parallel execution, but at the cost of reduced segmentation accuracy. These results demonstrate that AURASeg offers a reasonable accuracy–efficiency tradeoff where boundary precision is addressed, without compromising on its deployment in mobile robots. While AURASeg’s GFLOPs are higher due to the multi-stage APUD decoder and RBRM, it achieves the lowest parameter count (23.3M), indicating that the computational cost stems from spatial operations rather than model capacity, making it amenable to TensorRT FP16 optimization.

**Boundary Evaluation Protocol.** We compute Boundary IoU (BIOU) and Boundary F1 (BF1) by extracting a boundary band with morphological gradient operations (kernel size  $3 \times 3$ ), followed by  $k=2$  dilation iterations to tolerate minor spatial misalignment while penalizing larger boundary errors. The same protocol is applied consistently to all methods and both datasets.

**MIX Dataset (Gazebo+GMRPD).** AURASeg achieves the strongest boundary localization with BIOU=0.8124 and BF1=0.8905. Compared with the strongest baseline in this benchmark (UPerNet-R50: BIOU=0.7863, BF1=0.8738), this corresponds to relative improvements of 3.3% and 1.9%, respectively. Region-level metrics remain strong ( $\text{IoU}_{\text{drv}}=0.9897$ ,  $\text{F1}=0.9948$ ), showing that better boundaries do not compromise interior-region consistency.

**CARL-D Dataset.** On CARL-D, AURASeg also achieves the best overall performance:  $\text{IoU}_{\text{drv}}=0.8041$ ,  $\text{F1}=0.8914$ ,  $\text{BIOU}=0.0484$ , and  $\text{BF1}=0.0683$ . The lower absolute boundary values are attributable to CARL-D’s smooth polygon annotations, which produce far fewer boundary pixels ( $\sim 200$  vs.  $\sim 5000$  in MIX). AURASeg achieves relative improvements of 14.7% in BIOU and 9.5% in BF1 over the next-best method (PSPNet), demonstrating that boundary refinement remains effective even under annotation-limited evaluation. Despite this difference, AURASeg remains consistently superior, suggesting cross-domain generalization from robotic free-space to road-scene drivable-area seg-

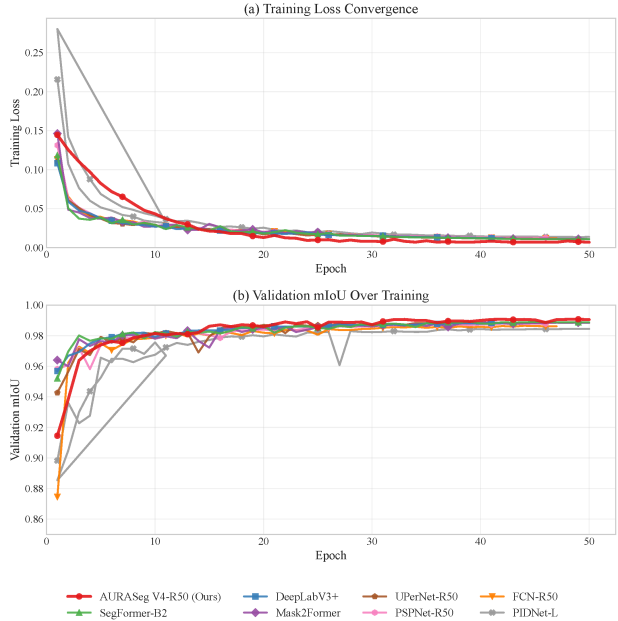


Figure 5. Training plots of AURASeg and baselines, showing stable convergence and improved validation performance for the proposed method.

mentation, especially considering boundary precision.

Fig. 4 compares RGB inputs, ground truth, and predictions on representative samples. Boundary error maps show that AURASeg produces cleaner and better-aligned free-space contours than competing methods, particularly near thin obstacles, floor–wall transitions, cluttered structures, and visually ambiguous free-space regions. As shown in Fig. 5, the model also converges rapidly and maintains a stable validation plateau under the unified training protocol.

## 5. Conclusion

Accurate drivable-area segmentation is essential for reliable mobile-robot navigation across indoor, outdoor, and road-scene environments. In this work, we present AURASeg, a compact encoder–decoder framework that combines lightweight multi-scale context aggregation (*ASPPLite*) with an *Attention-guided Progressive Upsampling Decoder* (APUD).

To explicitly address blurred or misaligned free-space boundaries, we introduce a *Residual Boundary Refinement Module* (RBRM) that learns boundary-sensitive features and injects them into the main stream through gated residual fusion. This design improves edge alignment without degrading interior-region stability. On the robot-centric MIX setting (Gazebo+GMRPD), AURASeg preserves strong region accuracy while improving boundary-centric metrics; robustness is further validated on the CARL-D road-scene

benchmark. In addition, on-device deployment and on-board evaluation indicate that AURASeg remains practical for edge robotic perception while delivering stronger boundary localization. Future work will study the integration of additional geometric cues, such as depth or motion, to further strengthen semantic segmentation in complex navigation scenarios.

## References

- [1] Liang-Chieh Chen, George Papandreou, Iasonas Kokkinos, Kevin Murphy, and Alan L. Yuille. Deeplab: Semantic image segmentation with deep convolutional nets, atrous convolution, and fully connected crfs. *arXiv preprint arXiv:1606.00915*, 2016. URL <https://arxiv.org/abs/1606.00915>. 1
- [2] Liang-Chieh Chen, George Papandreou, Florian Schroff, and Hartwig Adam. Encoder–decoder with atrous separable convolution for semantic image segmentation. In *European Conference on Computer Vision (ECCV)*, 2018. URL <https://arxiv.org/abs/1802.02611>. 1
- [3] S. Qu, Z. Wang, J. Wu, and Y. Feng. Fbrnet: A feature fusion and border refinement network for real-time semantic segmentation. *Pattern Analysis and Applications*, 27:22, 2024. doi: 10.1007/s10044-023-01207-2. 1, 2
- [4] C. Yu, J. Wang, C. Peng, C. Gao, G. Yu, and N. Sang. Bisenet: Bilateral segmentation network for real-time semantic segmentation. *arXiv preprint arXiv:1808.00897*, 2018. URL <https://arxiv.org/abs/1808.00897>. 1
- [5] Y. Wu, J. Jiang, and Y. Tian. Fpanet: Feature pyramid aggregation network for real-time semantic segmentation. *Applied Intelligence*, 2022. doi: 10.1007/s10489-021-02603-z. 1
- [6] H. Wang, X. Wang, J. Zhu, and Y. Yuan. Yolop: You only look once for panoptic driving perception. *International Journal of Automation and Computing*, 2022. 2
- [7] I. A. Kazerouni, G. Dooly, and D. J. F. Toal. Ghost-unet: An asymmetric encoder–decoder architecture for semantic segmentation from scratch. *IEEE Access*, 2021. doi: 10.1109/ACCESS.2021.3094925. 2
- [8] M. Nissar, A. K. Mishra, and B. K. Subudhi. Dual stream encoder–decoder architecture with feature fusion model for underwater object detection. *Mathematics*, 12(20), 2024. 2
- [9] J. Sun, L. Ma, and D. Zhao. Lcdnet: Lightweight context-aware depth estimation network. *arXiv preprint arXiv:2410.11580*, 2024. URL <https://arxiv.org/abs/2410.11580>. 2
- [10] Kaiming He, Xiangyu Zhang, Shaoqing Ren, and Jian Sun. Deep residual learning for image recognition. In *IEEE Conference on Computer Vision and Pattern Recognition (CVPR)*, 2016. doi: 10.1109/CVPR.2016.90. URL <https://arxiv.org/abs/1512.03385>. 2
- [11] Y. Li, X. Feng, and T. Wang. Depth-guided dpt: An efficient depth-aware semantic segmentation model. *arXiv preprint arXiv:2311.01966*, 2023. URL <https://arxiv.org/abs/2311.01966>. 2
- [12] M. A. M. Elhassan et al. S2-fpn: Scale-aware strip attention guided feature pyramid network for real-time semantic segmentation. *arXiv preprint arXiv:2206.07298*, 2022. doi: 10.48550/arXiv.2206.07298. URL <https://arxiv.org/abs/2206.07298>. 2
- [13] Q. H. Che, D. P. Nguyen, M. Q. Pham, and D. K. Lam. Twinlitenet: An efficient and lightweight model for driveable area and lane segmentation in self-driving cars. *arXiv preprint arXiv:2307.10705*, 2023. URL <https://arxiv.org/abs/2307.10705>. 2
- [14] Z. Wang, X. Guo, S. Wang, P. Zheng, and L. Qi. A feature refinement module for light-weight semantic segmentation network. *arXiv preprint arXiv:2412.08670*, 2024. URL <https://arxiv.org/abs/2412.08670>. 2
- [15] X. Qin, Z. Zhang, and C. Wang. Basnet: Boundary-aware semantic segmentation network. *arXiv preprint arXiv:2101.04704*, 2021. URL <https://arxiv.org/abs/2101.04704>. 2
- [16] J. Hyun, S. Woo, S. Lee, Y. Kim, and S. Ko. Street floor segmentation for a wheeled mobile robot. *IEEE Access*, 2022. doi: 10.1109/ACCESS.2022.3227203. 2
- [17] S. Zhou, X. Wang, and H. Wang. D-flow: A real-time optical flow estimation method. *arXiv preprint arXiv:2111.04525*, 2021. URL <https://arxiv.org/abs/2111.04525>. 2
- [18] Y. Zhang, K. Chen, and J. Luo. Agsl-free driving region detection using adaptive global structure learning. *Sensors*, 22(13), 2022. doi: 10.3390/s22134751. 2
- [19] Jie Hu, Li Shen, and Gang Sun. Squeeze-and-excitation networks. In *IEEE Conference on Computer Vision and Pattern Recognition (CVPR)*, 2018. doi: 10.1109/CVPR.2018.00745. URL <https://arxiv.org/abs/1709.01507>. 3
- [20] S. Woo, J. Park, J.-Y. Lee, and I. S. Kweon. Cbam: Convolutional block attention module. In *European Conference on Computer Vision (ECCV)*, 2018. URL <https://arxiv.org/abs/1807.06521>. 3
- [21] J. Wang, X. Li, and Y. Zhou. Gmrpd: Ground mobile robot perception dataset for drivable area segmentation. *arXiv preprint arXiv:2007.05950*, 2020. URL <https://arxiv.org/abs/2007.05950>. 5
- [22] M. A. Butt and F. Riaz. Carl-d: A vision benchmark suite and large scale dataset for vehicle detection and scene segmentation. *Signal Processing: Image Communication*, 104: 116667, 2022. doi: 10.1016/j.image.2022.116667. 5
- [23] Jonathan Long, Evan Shelhamer, and Trevor Darrell. Fully convolutional networks for semantic segmentation. In *IEEE Conference on Computer Vision and Pattern Recognition (CVPR)*, 2015. doi: 10.1109/CVPR.2015.7298965. URL <https://arxiv.org/abs/1411.4038>.
- [24] H. Zhao, J. Shi, X. Qi, X. Wang, and J. Jia. Pyramid scene parsing network. In *IEEE Conference on Computer Vision and Pattern Recognition (CVPR)*, 2017. doi: 10.1109/CVPR.2017.660. URL <https://arxiv.org/abs/1612.01105>.
- [25] T. Xiao, Y. Liu, B. Zhou, Y. Jiang, and J. Sun. Unified perceptual parsing for scene understanding. In *European Conference on Computer Vision (ECCV)*, 2018. URL <https://arxiv.org/abs/1807.10221>.

- [26] E. Xie et al. Segformer: Simple and efficient design for semantic segmentation with transformers. In *Advances in Neural Information Processing Systems (NeurIPS)*, 2021. URL <https://arxiv.org/abs/2105.15203>.
- [27] B. Cheng, I. Misra, A. G. Schwing, A. Kirillov, and R. Girshik. Masked-attention mask transformer for universal image segmentation. In *IEEE/CVF Conference on Computer Vision and Pattern Recognition (CVPR)*, 2022. URL <https://arxiv.org/abs/2112.01527>.
- [28] J. Xu et al. Pidnet: A real-time semantic segmentation network inspired by pid control. In *IEEE/CVF Conference on Computer Vision and Pattern Recognition (CVPR)*, 2023. URL <https://arxiv.org/abs/2206.11430>.